Derivation and Evaluation of a New Extinction Coefficient for Use With the n-HUT Snow Emission Model

William Maslanka, Melody Sandells, Robert Gurney, Juha Lemmetyinen, Leena Leppänen, Anna Kontu, Margret Matzl, Nick Rutter, Tom Watts, and Richard Kelly

***Abstract*— In this study, snow slab data collected from the Arctic Snow Microstructure Experiment were used in conjunction with a six-directional flux coefficient model to calculate individual slab absorption and scattering coefficients. These coefficients formed the basis for a new semiempirical extinction coefficient model, using both frequency and optical diameter as input parameters, along with the complex dielectric constant of snow. Radiometric observations, at 18.7, 21.0, and 36.5 GHz at both horizontal polarization (H-Pol) and vertical polarization (V-Pol), and snowpit data collected as part of the Sodankylä Radiometer Experiment were used to compare and contrast the simulated brightness temperatures produced by the multi-layer Helsinki University of Technology snow emission model, utilizing both the original empirical model and the new semiempirical extinction coefficient model described here. The results show that the V-Pol RMSE and bias values decreased when using the semiempirical extinction coefficient; however, the H-Pol RMSE and bias values increased on two of the lower microwave bands tested. The unbiased RMSE was shown to decrease across all frequencies and polarizations when using the semiempirical extinction coefficient.**

***Index Terms*— Extinction coefficient modeling, HUT snow emission model, microwave scattering, remote sensing, snow emission model.**

I. Introduction

SNOW is a vitally important variable in numerous meteorological and climatological processes, because of its high albedo, thermal emissivity, and thermal insulating properties [1]. In addition to this, over one billion people rely on glacier and snowmelt for their freshwater drinking supply [2], making estimations of snow mass vital for hydrological forecasts. To monitor the global snow water equivalent (SWE), passive microwave remote sensing methods have been utilized over the last 30 years [3]–[6] due to the all-weather capability and illumination independence that is offered by passive microwave remote sensing techniques [7]–[9]. Passive microwave remote sensing is a viable method of global snow mass monitoring, due to the interactions between upwelling microwave radiation and snow crystals.

Observed microwave radiation of the snowpack is comprised of two contributions, from the underlying surface and from the snowpack itself. An additional atmospheric contribution must be considered when using spaceborne sensors [9]. Snow crystals within the snowpack act as scattering centers for the upwelling microwave radiation, meaning that the microwave signature of the snowpack is highly sensitive to the snow crystal size, the snow mass, and the radiation wavelength (and therefore its frequency [3], [10]).

Recently, semiempirical models such as the multi-layer Helsinki University of Technology (n-HUT) snow emission model [11], [12] have been used in conjunction with passive microwave remote sensing data in order to extract snow information from satellite observations [13]. The n-HUT snow emission model is based on radiative transfer theory, treating the snowpack as a series of homogeneous layers. The basic assumption of the n-HUT model is that scattering is mostly concentrated in the forward direction, with the fraction of scattered radiation being empirically set to 0.96 [11]. The original HUT model neglects the backward scattered radiation in the radiative transfer function. It has been shown that for deep snowpacks, this may lead to increasing the underestimation of brightness temperature with the HUT model when compared to a more complete two-directional flux treatment of microwave propagation [14]. The absorption coefficient is calculated from the complex dielectric constant of dry snow, determined from the formulas given by Mätzler [15] and [16]. The extinction properties of dry snow were originally calculated as a function of both frequency and grain size, as shown in [10].

For manual characterization of snowpack parameters, observers often describe the microstructure of the individual layers by the grain size of its ice particles, E, defined as "'the size of the average grains," where the size of the grains is "'its greatest extension measured in millimeters" [17]. The conventional method for observing the grain size of

Manuscript received March 1, 2018; revised July 25, 2018, October 29, 2018, and February 13, 2019; accepted March 12, 2019. Date of publication June 6, 2019; date of current version September 25, 2019. This work was supported by the EU 7th Framework Program Project "European–Russian Centre for Cooperation in the Arctic and Sub-Arctic Environmental and Climate Research" (EuRuCAS) under Grant 295068. *(Corresponding author: William Maslanka.)*

W. Maslanka is with the Department of Geography and Environmental Sciences, University of Reading, Reading, U.K. (e-mail: will.maslanka@googlemail.com).

M. Sandells is with the Centre for Open Research (CORES) in Engineering and Science Ltd., Tyne and Wear NE39 2JA, U.K.

R. Gurney is with Department of Meteorology, University of Reading, Reading, U.K.

J. Lemmetyinen, L. Leppänen, and A. Kontu are with the Artic Research Center, Finish Meteorological Institute, 99600 Sodankylä, Finland.

M. Matzl is with the WSL Institute for Snow and Avalanche Research SLF, 7260 Davos Dorf, Switzerland.

N. Rutter and T. Watts are with the Department of Geography and Environmental Sciences, Northumbria University, Newcastle upon Tyne, U.K.

R. Kelly is with the Department of Geography and Environmental Management, University of Waterloo, Waterloo, ON, Canada.

Color versions of one or more of the figures in this article are available online at http://ieeexplore.ieee.org.

Digital Object Identifier 10.1109/TGRS.2019.2913208

0196-2892 © 2019 IEEE. Translations and content mining are permitted for academic research only. Personal use is also permitted, but republication/redistribution requires IEEE permission. See http://www.ieee.org/publications_standards/publications/rights/index.html for more information.

a snowpack layer is done, by placing a sample of snow grains onto a millimeter grid and visually estimating the grain size either through the use of a pocket microscope or through macrophotography and image processing [18]. Advanced methods for quantifying the 3-D size of the individual snow grains have also been implemented [19].

Observations of the grain size in the field are subjected to numerous different sources of error. The preparation of the snow grains upon the millimeter grid introduces a random error to the observation through the arbitrary selection of grains for the sample, while the measurement technique introduces the potential for observer-related errors, discussed by Leppänen *et al.* [20]. Three individual observers analyzed macrophotographs relating to a single snowpack profile of grain size. Leppänen *et al.* [20] showed that an observer-related error of at least 0.25 mm was present, with samples of larger grains producing larger observer-related errors.

The specific surface area (SSA) is a separate microstructure parameter that has been under increased focus over the past decade [21]. SSA is defined as the total area at the ice/air interface per unit mass [22] or as the total area at the ice/air interface per unit volume [23], and can be observed for a snowpack via numerous different techniques, observed in the field using integrating sphere reflectance measurements, such as dual-frequency integrating sphere for snow SSA (DUFISSS) measurement [24], IceCube [25], and IRIS [23], penetrometry measurements [26]–[28], gas adsorption techniques [22], and computer tomography analysis [29], [30]. SSA is inversely proportional to the optical diameter, D_o, defined as the diameter of a sphere with that shares the same SSA to that of the snow in question, regardless of the shape of the grains, and is calculated by

$$D_o = \frac{6}{\rho_{\text{ice}}\text{SSA}} \tag{1}$$

where SSA is measured in $\text{m}^2 \cdot \text{kg}^{-1}$ and $\rho_{\text{ice}} = 917\ \text{kg} \cdot \text{m}^{-3}$. Unlike grain size, which is subject to observer-related errors, D_o is a well-defined variable that can be calculated directly from observations of SSA through (1).

This paper uses the data collected as part of the Arctic Snow Microstructure Experiment (ASMEx, [31], [32]) to derive a new semiempirical extinction coefficient for snow, using optical diameter rather than grain size as an input parameter, for use within the n-HUT model. This approach is novel, as a flux coefficient model has been utilized to produce an extinction coefficient model for use within the n-HUT model using optical diameter (derived from measurements of SSA) as a direct input, rather than the traditional grain size. Section II details the ASMEx campaign and briefly describes the data collected. Section III details the flux coefficient model, in which the absorption and scattering coefficients are calculated from the ASMEx data. Section IV shows the derivation of the semiempirical extinction model, with its implementation and evaluation being shown in Section V.

II. Arctic Snow Microstructure Experiment

To derive a new semiempirical extinction coefficient model, the radiometric and snow characteristic data of the

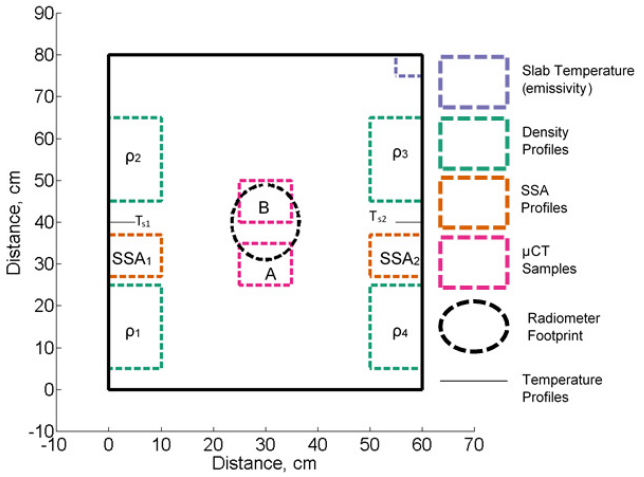


Fig. 1. Approximate locations of the radiometric, macrostructure, and microstructure observations of the ASMEx snow slabs. Individual μCT subsample locations are also shown. Adapted from [31] and [32].

ASMEx [31], [32] were used. The radiometric observations included observations of extracted snow slabs of approximately $80 \times 80 \times 15$ cm^2, extracted from naturally accumulated taiga snow, upon two bases with different radiometric properties, a reflective metal plate (a near-perfect reflector, interface reflectivity $= 1$) and an absorptive blackbody base (a near-perfect absorber, interface reflectivity $= 0$), similar to those in [33] and [34]. Radiometric observations were made at an incidence angle of 50° to the vertical at 18.7, 21.0, 36.5, 89.0, and 150.0 GHz, at both horizontal polarization (H-Pol) and vertical polarization (V-Pol). The reflective metal plate and the absorptive blackbody base were both allowed to acclimatize to the ambient physical air temperature of the snow, prior to the radiometric observations, to reduce the risk of the snow melting and refreezing to the bases during the observations [32]. Observations of the downwelling sky radiation at all available frequencies and at both polarizations were made immediately after the radiometric observations of the snow slabs, in order to observe any changes in environmental downwelling radiation. Upon the completion of all radiometric observations, the physical properties of the snow were characterized using the conventional snowpit observation techniques (as described by Leppänen *et al.* [18]) as well as by X-ray computer tomography (μCT, [29], [30]). This allowed for both conventional and modern observation techniques (in the case of microstructure parameterization, and subjective and objective observation techniques, respectively) to be used. Fig. 1 shows the approximate location of all physical observations made across the ASMEx slabs, as well as the calculated location of the radiometric footprint. Prior to the ASMEx campaign, iterative measurements of a reflective metal sheet upon the absorbing blackbody material were completed, in order to empirically find the dimensions of the radiometer footprint and the effects and positions of the associated sidelobes. The center of the Styrofoam positioner was very sensitive to the metallic strip, while the edges of the Styrofoam were hard/not sensitive to the metallic strip, thus highlighting the location of the footprint.

This field of view characterization was drawn upon a "Styrofoam positioner" used throughout the ASMEx campaign

(see [32, Fig. 3.5]) to allow for numerous snow slabs to be observed from the same location, thus keeping the radiometric footprint within the snow slabs. This could produce a potential source of error, as misalignment of the snow slabs with the positioner markings could result in different parts of the snow slab, or even the plastic support box, being present in the field of view. A second potential source of error is present, due to the fact that the snow slabs were not in the far field of the radiometers, due to the practicalities of the ASMEx campaign; however, determining the impact of this error could not be calculated without careful analysis, which is beyond the scope of this study.

III. Flux Coefficient Model

A. Deriving Slab Reflectivities and Transmissivities

The ASMEx observations were designed to measure the absorption and scattering properties of the extracted snow slabs. This was done by calculating the emissivity, reflectivity, and transmissivity of the extracted snow slabs using the observed microwave brightness temperatures of snow slabs upon the reflective metal base (T_{BM}) and upon the absorptive blackbody base (T_{BA}), as well as the snow slabs physical temperature (T_{phys}) and the downwelling sky radiation (T_{BSKY}). In order to calculate the absorption and scattering properties of the snow slabs, a flux coefficients model based on a six-directional sandwich model, first detailed by Wiesmann *et al.* [33], was used.

T_{BM} and T_{BA} are comprised of two individual sources, from the emission by the snow slab itself (governed by its physical temperature T_{phys}) and from the downwelling sky radiation reflected by the snow slab and base (where the total reflectivity are r_{met} and r_{abs}, respectively). T_{BM}, therefore, is equal to

$$T_{\mathrm{BM}} = (1 - r_{\mathrm{met}})T_{\mathrm{phys}} + r_{\mathrm{met}}T_{\mathrm{BSKY}} \tag{2}$$

while T_{BA} is equal to

$$T_{\mathrm{BA}} = (1 - r_{\mathrm{abs}})T_{\mathrm{phys}} + r_{\mathrm{abs}}T_{\mathrm{BSKY}}. \tag{3}$$

The total reflectivity of the snow upon the reflective metal plate and absorptive blackbody base (accounting for coherent wave interactions within the slab) is related to the internal reflectivities (r) and transmissivities (t), as well as the Fresnel reflectivities (r_i), which is expressed as

$$r_{\mathrm{met}} = r_i + (1 - r_i)^2 R_{\mathrm{met}} \tag{4}$$

$$r_{\mathrm{abs}} = r_i + (1 - r_i)^2 R_{\mathrm{abs}} \tag{5}$$

where R_{met} and R_{abs} are functions of r, t, and r_i

$$R_{\mathrm{met}} = \frac{r + t^2(1 - r)^{-1}}{1 - rr_i - r_i t^2(1 - r)^{-1}} \tag{6}$$

$$R_{\mathrm{abs}} = \frac{r + r_i t^2(1 - rr_i)^{-1}}{1 - rr_i - (r_i t)^2(1 - rr_i)^{-1}}. \tag{7}$$

Fig. 2 shows a schematic of the snow slab upon the base (either blackbody absorbing or the metal reflective base). The internal reflectivities, internal reflectivities, Fresnel reflectivities, and total reflectivity of the slab upon different bases are shown for clarity.

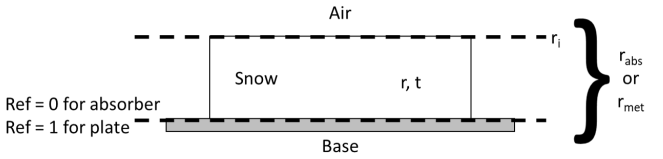


Fig. 2. Schematic of the snow slab upon a material base (either a blackbody absorber or reflective metal base, detailing the numerous distinctive reflectivities used in (4)–(7).

R_{met} and R_{abs} can be calculated from evaluated values of r_{abs} and r_{met}, respectively [using (2) and (3)], if the value of r_i is known. As the snow interface was considered to be smooth, r_i was assumed to be equal to that of the Fresnel reflectivity. The Fresnel reflectivity was determined from the incidence angle and complex dielectric constant ε (where $\varepsilon = \varepsilon' + i\varepsilon''$).

By solving (6) and (7), r and t of the individual slabs can be obtained. Rearranging (6) and (7) gives a pair of nonlinear equations for the internal reflectivity and transmissivity of the slabs

$$r = R_{\mathrm{abs}}(1 - rr_i - (r_i t)^2(1 - rr_i)^{-1}) - r_i t^2(1 - rr_i) \tag{8}$$

$$t^2 = R_{\mathrm{met}}((1 - rr_i)(1 - r) - r_i t^2) - r(1 - r) \tag{9}$$

where the values of R_{abs}, R_{met}, and r_i are known. Wiesmann *et al.* [33] proposed an iterative solution to (8) and (9), by setting $r_i = 0$ for the first iteration

$$r = R_{\mathrm{abs}}; \quad t^2 = (R_{\mathrm{met}} - R_{\mathrm{abs}})(1 - R_{\mathrm{abs}}). \tag{10}$$

This gave a first iterative solution for (8) and (9). Inserting the first iterative solution back into the pair of nonlinear equations, with the calculated value of r_i gave a second iterative solution. This process was repeated until the old and new values varied by less than 0.0005.

B. Deriving Absorptive and Scattering Properties of Slabs

To link r and t to the absorption and scattering properties of the snow slabs, the six-directional flux coefficient model, developed by Wiesmann *et al.* [33] and used by Toure *et al.* [34], was applied. The six-directional flux coefficient model accounts for the radiation propagating through the snow slab along the three principal axes, for a given frequency and polarization. Radiation propagating in the four horizontal directions represents the internally trapped radiation, whose internal incidence angle θ is greater than the critical angle θ_c

$$\theta > \theta_c = \arcsin\left(\frac{1}{\sqrt{\varepsilon'}}\right). \tag{11}$$

The vertical fluxes depict those that were not subject to a total internal reflection. For isotropic and plane-parallel snow slabs, the six-flux model is transformed into a traditional two-flux model, where two-flux absorption (γ_a') and scattering (γ_b') coefficients are written in terms of the six-flux parameters

$$\gamma_a' = \gamma_a(1 + 4\gamma_c(\gamma_a + 2\gamma_c)^{-1}) \tag{12}$$

$$\gamma_b' = \gamma_b + 4\gamma_{c2}(\gamma_a + 2\gamma_c)^{-1} \tag{13}$$

where γ_a is the six-flux absorption coefficient, γ_b is the six-flux backscattering coefficient, and γ_c is the six-flux scattering coefficient around 90° (perpendicular to the direction

of travel). Wiesmann *et al.* [33] stated that r and t of a snow slab with thickness d could be calculated via

$$r = r_0\left(1 - t_0^2\right)\left(1 - r_0^2 t_0^2\right)^{-1} \tag{14}$$

$$t = t_0\left(1 - r_0^2\right)\left(1 - r_0^2 t_0^2\right)^{-1} \tag{15}$$

where the one-way transmissivity through the slab, t_0, is calculated via

$$t_0 = \exp\left(\frac{-\gamma\, d}{\cos\theta}\right) \tag{16}$$

and where the reflectivity of infinite slab thickness, r_0, is calculated via

$$r_0 = \gamma_b'\left(\gamma_a' + \gamma_b' + \gamma\right)^{-1}. \tag{17}$$

Both r_0 and t_0 are calculated through a function of γ_a', γ_b', and the dampening coefficient γ

$$\gamma = \sqrt{\gamma_a'\left(\gamma_a' + 2\gamma_b'\right)}. \tag{18}$$

Wiesmann *et al.* [33] used a number of iterative processes to calculate the values of r_0 and t_0, in order to calculate the two-flux absorption and scattering coefficients, initially from values of R_{met} and R_{abs}.

In order to link the calculated values of r and t to those of r_0 and t_0, and thus to the six-flux coefficients, a second iterative process was used. Equations (14) and (15) were rearranged to form another set of nonlinear equations

$$r_0 = \frac{-1 + \sqrt{1 + 4G^2}}{2G};\quad G \equiv \frac{r_0}{1 - r_0^2} = \frac{r}{t}\frac{t_0}{1 - t_0^2} \tag{19}$$

$$t_0 = t\left(1 + r_0^2\left(1 - t_0^2\right)\left(1 - r_0^2\right)^{-1}\right). \tag{20}$$

Setting $t_0 = t$ allowed for a first iterative solution to be found for r_0 and t_0. Similar to the first iterative process, the iterative solutions were fed into the nonlinear equations repeatedly until the old and new values converged to within 0.0005. The values of γ_a' and γ_b' were calculated using rearranged forms of (17) and (18)

$$\gamma_a' = \gamma\,\frac{1 - r_0}{1 + r_0} \tag{21}$$

$$\gamma_b' = \left(\gamma + \gamma_a'\right)\frac{r_0}{1 - r_0} \tag{22}$$

where γ was calculated using (16). For isotropic scattering by snow crystals, the total six-flux scattering coefficient, γ_s, is given by

$$\gamma_s = 2\gamma_b + 4\gamma_c \tag{23}$$

and the ratio between γ_b and γ_c is given by

$$\frac{2\gamma_c}{\gamma_b} = \frac{x}{1 - x} \tag{24}$$

where

$$x = \sqrt{\frac{\varepsilon' - 1}{\varepsilon'}}. \tag{25}$$

The full set of six-flux coefficients (γ_a, γ_b, γ_c, and γ_s) can now be calculated from the values of the two-flux coefficients [using (12) and (13)], the complex dielectric constant of the snow slabs, and (21)–(25). By solving (2)–(25), using the ASMEx radiometer data and μCT observed bulk slab data, the ASMEx six-flux absorption and scattering coefficients were calculated.

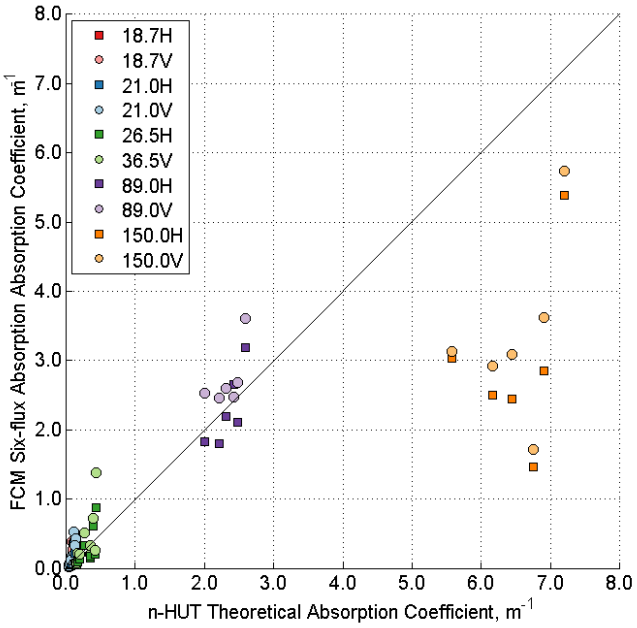


Fig. 3. of the retrieved absorption coefficient γ_a and the n-HUT theoretical absorption coefficient $k_{a,\text{HUT}}$ at 18.7 (red), 21.0 (blue), 36.5 (green), 89.0 (purple), and 150.0 (orange) GHz, at both H-Pol (square, bold) and V-Pol (circle, pale).

The impact of the snow slabs not being in the far field is difficult to assess without careful analysis, which was beyond the scope of this study. Many parts of the six-flux model (such as total internal reflection) assumes planar waves, which is not entirely valid, and thus may introduce some discrepancies. For this study, these discrepancies have been neglected.

IV. Semiempirical Extinction Coefficient Calculation

The ASMEx radiometric, bulk physical characteristics and μCT bulk microstructure slab data were used with the flux coefficient model described in Section III, to produce values of γ_a and γ_s, for each individual ASMEx slab. Fig. 3 shows a comparison of all calculated γ_a values with the equivalent absorption coefficient, calculated using the n-HUT model [$k_{a,\text{HUT}}$, (26)]

$$k_{a,\text{HUT}} = \left(4\pi\left(F \times 10^9\right)\right)\left(\sqrt{\mu_0\varepsilon_0\varepsilon_{\text{snow}}'}\right) \times \left(\sqrt{0.5\left(\sqrt{1 + \left(\frac{\varepsilon_{\text{snow}}''}{\varepsilon_{\text{snow}}'}\right)^2}\right) - 1}\right) \tag{26}$$

where F is the frequency (GHz), μ_0 is the permeability of free space ($4\pi \times 10^{-7}$ H$\cdot$m^{-1}), ε_0 is the permittivity of free space (8.85×10^{-12} F$\cdot$m^{-1}), and $\varepsilon_{\text{snow}}'$ and $\varepsilon_{\text{snow}}''$ are the real and imaginary dielectric constants of dry snow, respectively. $\varepsilon_{\text{snow}}'$ and $\varepsilon_{\text{snow}}''$ are calculated internally within the n-HUT model, using formulas given in [15] and [35], with the latter using a Polder-van Santen mixing model.

All γ_a and $k_{a,\mathrm{HUT}}$ values were calculated at all available frequencies, at both H-Pol and V-Pol, for each ASMEx slab. It is clear that for the lower four frequencies, the values of γ_a are similar to that of the equivalent $k_{a,\mathrm{HUT}}$ values, while at 150.0 GHz, the values of γ_a underestimate the equivalent $k_{a,\mathrm{HUT}}$ values. The coefficient of determination, R^2, the value of the γ_a values using the lower four frequencies at V-Pol is 0.945, while the R^2 value using all V-Pol γ_a is lower (0.765). This suggests that the flux coefficient model has issues retrieving flux coefficients at 150.0 GHz. This is due to the extinction processes being dominated by surface processes. The small penetration depth at 150 GHz results in the emitted microwave radiation from the blackbody base or the reflected microwave radiation from the reflecting base being effectively scattered by the snow before the radiation leaves the snowpack from the surface. Thus, due to the small penetration depth at 150.0 GHz, the presented methodology could not be applied at 150.0 GHz.

The closeness of the retrieved γ_a values to the $k_{a,\mathrm{HUT}}$ values in the lower four frequencies (Fig. 3) suggests that the flux coefficient model retrieves accurately the absorption coefficients. For the ease of implementation within the n-HUT model, the absorption coefficient term of the new extinction coefficient was equal to that of the theoretical absorption coefficient already used by the n-HUT model.

The retrieved V-Pol six-flux scattering coefficients, calculated from the ASMEx slabs, were used to form the scattering coefficient term of the newly derived extinction coefficient. The H-Pol was seen to be more readily effected by layer and discontinuities within the snowpack and was, thus, not used in the scattering coefficient calculation. The scattering coefficient term, using the optical diameter observations, was hypothesized to be in the form

$$\gamma_s = \alpha (D_0)^{c1} (F)^{c2} \tag{27}$$

where c_1 and c_2 are the exponents of the optical diameter and frequency, respectively, and α is a multiplication factor. To calculate the value of c_2, α and the optical diameter dependency can be combined to make $\beta = \alpha\ (D_0)^{c1}$. As the value of β is independent of the value of c_2, the values of β were normalized, in order to determine the value of c_2. Fig. 4 shows plotted regression lines using V-Pol γ_s ASMEx values, in the form detailed by (27), setting $\beta = 1$.

After normalizing the ASMEx V-Pol γ_s regression lines, a common band of frequency exponents was visible, in the range $1.81 < c_2 < 2.55$. Fig. 5 indicates that this common band of frequency exponents is due to the number of frequency observations made and not the homogeneity of the slabs. The μCT profiles of D_o of each individual slab were assessed, and the standard deviation of each D_o profile was calculated. If the standard deviation of each D_o profile was below a threshold value of 0.15 mm, the slab was characterized as homogeneous. This standard deviation threshold was used for each slab with the exception of slab A03, which was deemed as "wet" [31], [32] and subsequently characterized as nonhomogeneous. The regression laws shown in Fig. 4 were calculated using the bulk value of D_o, calculated from SSA values observed using the μCT analysis. To calculate a mean value of c_2 from the common band of frequency exponents, a threshold region of $1 < c_2 < 3$ was chosen, highlighted in blue in Fig. 4. The mean c_2 value within the threshold region was calculated to be 2.12, highlighted in red in Fig. 4.

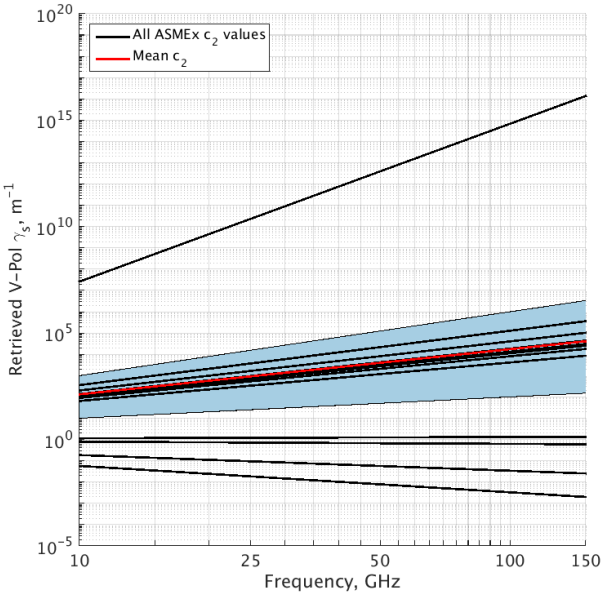


Fig. 4. Frequency regression lines of retrieved V-Pol scattering coefficients γ_s for all ASMEx snow slabs. Regression lines were calculated and plotted in the form $\gamma_s = \beta(F)^{c1}$. The blue-shaded area denotes the threshold region, while the regression line plotted in red shows the mean c_2 value.

The value of c_1 was calculated in a similar fashion to that of c_2, by rearranging (27) such that α and the frequency dependency were combined to make $\Phi = \alpha(F)^{c2}$, and then normalizing the resulting expression, as Φ is independent of c_1. Fig. 6 shows the optical diameter regression laws (using $\Phi = 1$), using the V-Pol γ_s ASMEx values, at each of the five observed frequencies.

Unlike with the frequency regression laws, a common optical diameter exponent band is not present within Fig. 6, due to the small selections of individual frequencies. Analysis of the slab homogeneity and number of observations (similar to that of the frequency regression laws in Fig. 5) did not offer a clear indication regarding a common optical diameter exponent band. The 150.0-GHz regression law was not used in the calculation of the optical diameter exponent c_1, as the extinction properties at this frequency were dominated by surface processes due to the limiting penetration depth (as shown by the absorption coefficient retrieval in Fig. 3). Therefore, a mean value of c_1 was determined for the regression laws of 18.7–89.0 GHz, giving c_1 to be 2.12.

After the calculation of both c_1 and c_2, the value of α was determined by plotting all retrieved values of γ_s against calculated values of $(D_o)^{c1}(F)^{c2}$. A regression law was then calculated, setting the regression law intercept to the origin (as scattering tends to zero as snow crystal diameter decreases). Fig. 7 shows the retrieved γ_s values against calculated values of $(D_o)^{c1}(F)^{c2}$, as well as the resulting regression law, whose gradient, and thus α, is 0.0065 $\mathrm{m}^{-1}\cdot\mathrm{mm}^{-2.12} \cdot \mathrm{GHz}^{-2.12}$.

After the calculation of α, c_1, and c_2, the exponents and multiplication factor were substituted into (27), in order

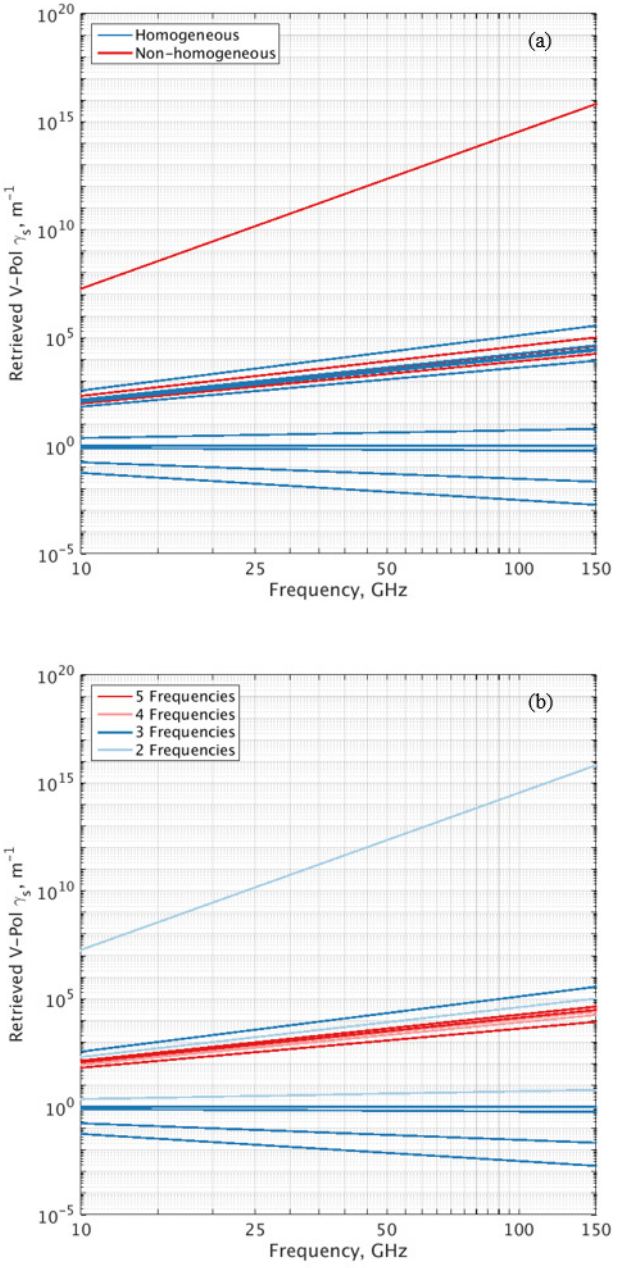


Fig. 5. ASMEx γs frequency regression lines, denoting (a) homogeneous (blue) and nonhomogeneous (red) slabs, using μCT properties to denote homogeneity, and (b) number of frequency observations used to calculate the regression lines; 5 (dark red), 4 (light red), 3 (dark blue), and 2 (light blue).

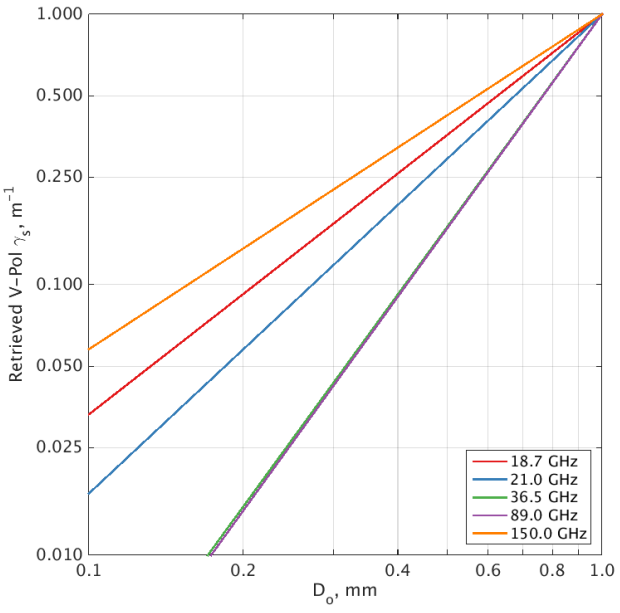


Fig. 6. Optical diameter D_o regression lines of V-Pol γ_s for all frequencies used during ASMEx. Regression lines were calculated and plotted in the form $\Phi = \alpha(F)^{c2}$. Frequencies shown are 18.7 (red), 21.0 (blue), 36.5 (green), 89.0 (purple), and 150.0 (orange) GHz.

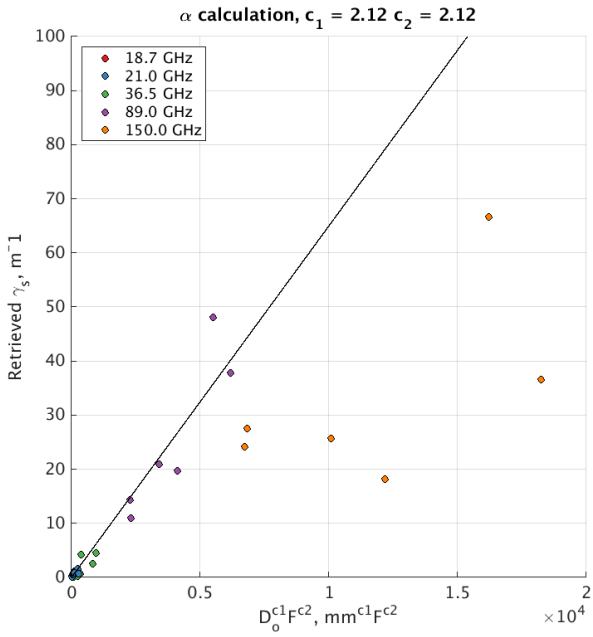


Fig. 7. Regression line comparing the retrieved values of the scattering coefficient γ_s against calculated values of $(D_o)^{c1}(F)^{c2}$ at 18.7 (red), 21.0 (blue), 36.5 (green), 89.0 (purple), and 150.0 (orange) GHz. The gradient on the plotted regression law denotes the value of α (0.0065 m^{-1} · mm$^{-2.12}$ · GHz$^{-2.12}$).

to form an empirical scattering coefficient. Fig. 8 shows a comparison of the retrieved six-flux scattering coefficient, using the flux coefficient model, with the empirical scattering coefficient model [calculated with (27)]. It can be seen that for the lower four ASMEx frequencies, the empirical scattering coefficient accurately calculates the scattering coefficient, with a calculated R^2 value of 0.933 for the calculations in the range 18.7–89.0 GHz. The calculations at 150.0 GHz, however, produce a large overestimation of scattering coefficient; a fact that can be seen as the calculated value of R^2 for all points is lower (0.637) than that of just the lower four frequencies (0.933). The empirical scattering coefficient calculated above can be implemented into the n-HUT model, using the pre-existing theoretical absorption coefficient, in order to produce a semiempirical extinction coefficient

$$k_e = (4\pi(F \times 10^9))\left(\sqrt{\mu_0\varepsilon_0\varepsilon'_{\text{snow}}}\right) \times \left(\sqrt{0.5\left(\sqrt{1+\left(\frac{\varepsilon''_{\text{snow}}}{\varepsilon'_{\text{snow}}}\right)^2}\right)-1}\right) + 0.0065(D_o)^{2.12}(F)^{2.12}. \quad (28)$$

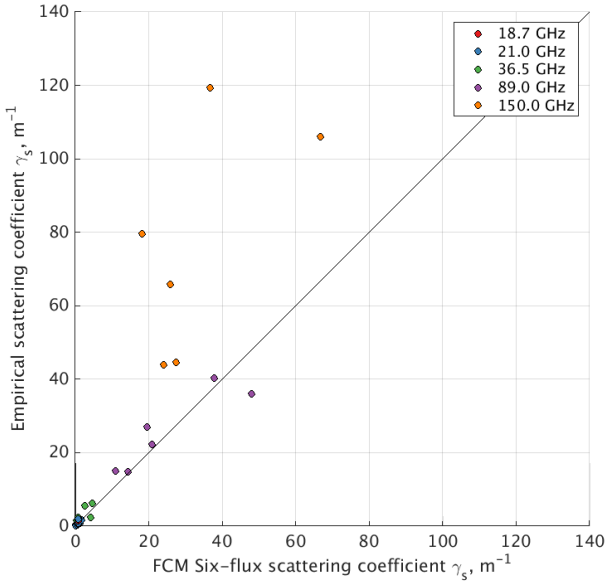


Fig. 8. Comparison of the retrieved values of the scattering coefficient γ_s using the flux coefficient model as detailed in [33] with values of γ_s calculated using (28), at 18.7 (red), 21.0 (blue), 36.5 (green), 89.0 (purple), and 150.0 (orange) GHz, at V-Pol. R^2 was calculated to be 0.637 across all five frequencies used and 0.933 for the range 18.7–89.0 GHz.

TABLE I
CHANGE IN RMSE AND BIAS FOR ASMEX SLABS

Frequency	RMSE (K)	Bias (K)
18.7	0.26	-0.65
21.0	0.21	-0.97
36.5	0.03	-8.23
89	-21.59	-36.89

V. EVALUATION OF SEMIEMPIRICAL COEFFICIENT WITH SODANKYLÄ RADIOMETER EXPERIMENT

As an intermediate step to test the new extinction coefficient, n-HUT was used to simulate the brightness temperature of the snow slabs over the metal plate and over the absorber. Two sets of simulations were performed: first with the original extinction coefficient model given the traditional (subjective) grain size observations, and second, the new extinction coefficient model given in this paper and driven by optical grain diameter derived from μ CT observations. Identical cutter densities were used in both sets of simulations. The changes in RMSE and bias [see (29) and (30)] from the original extinction coefficient to the new are shown in Table I.

In order to evaluate the n-HUT model with independent observations of a full snowpack, simulated brightness temperatures (using both the original and the new extinction coefficients) were compared to observed brightness temperatures, using data collected as part of the Sodankylä Radiometer Experiment (SoRaX). SoRaX consisted of numerous radiometric and snow property observations of the multiple layered snowpacks within the intensive observation area (IOA) at the Finnish Meteorological Institute Arctic Research Centre

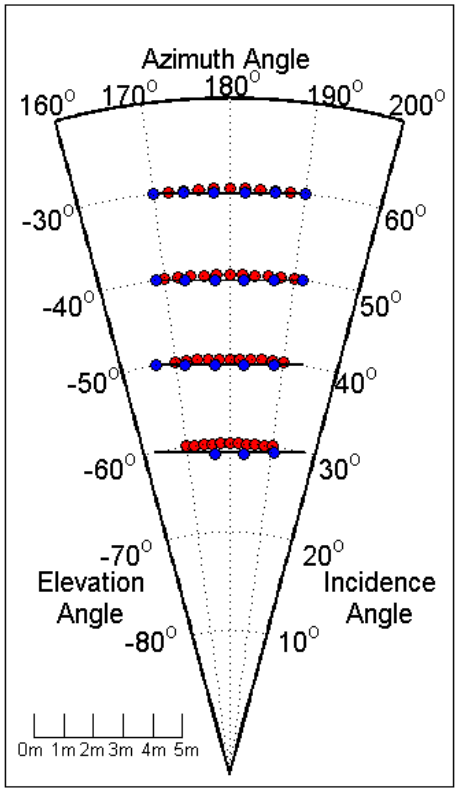


Fig. 9. Azimuth and elevation angles of all radiometric (red) and snowpit (blue) observations in the SoRaX snow characterization campaign. The snowpit observations were spaced 1 m apart. The black horizontal line denotes the location of snow trenches and NIR photographs. Equivalent incidence angles are also shown alongside the corresponding elevation angle.

(FMI ARC), Sodankylä, Finland. Radiometric observations at 18.7, 21.0, and 36.5 GHz were made at a range of azimuth and elevation angles (Fig. 9). Radiometers were calibrated prior to the observations using both ambient temperature calibration observations were aligned with the nearest profiles. Table II shows the radiometric azimuth and elevation angles corresponding to each SoRaX snow trench used. Profiles at 0 and 5 m for the −50° elevation angle snow trench were not utilized in this analysis, as the center of radiometric footprints was not deemed to be close enough to the SoRaX snowpits. Snow microstructure profiles within the −40° and −50° elevation angle snow trenches were chosen for simulation with the n-HUT model. The following observations of snow microstructure were made in each trench: a trench-long near-infrared (NIR) photograph composite for stratigraphic analysis [36], individual physical temperature (Ts) profiles, snow density (ρ_s) profiles using a 500-mL box cutter [18], [27], SSA profiles using an IceCube instrument [24], [25], grain size (E) profiles via macrophotography analysis [18], layer thickness (L), and total snow height (HS) observations. Table III shows how measurement profiles were located in each trench. Where profiles did not have observations (e.g., physical temperature or visually determined traditional grain size), mean profiles were used from observations across the trench.

Snowpack stratigraphy in the −40° and −50° elevation trenches was input into the n-HUT model, using both the original extinction coefficient ([10], using visually determined

TABLE II
AZIMUTH ANGLES ASSOCIATED WITH SNOWPIT OBSERVATIONS MADE ACROSS −40° AND −50° ELEVATION ANGLES OF THE SORAX CAMPAIGN

Ele.	0 m	1 m	2 m	3 m	4 m	5 m
-40º	190	186	182	178	174	170
-50º	N/A	188	182	178	172	N/A

TABLE III
SORAX SNOWPIT AND SNOW TRENCH OBSERVATIONS

Ele.	Obs	0 m	1 m	2 m	3 m	4 m	5 m
	NIR	X	X	X	X	X	X
	T_s	X	X			X	X
	ρ	X	X	X	X	X	X
-40º	*SSA*	X	X		X	X	X
	E				X		
	HS	X	X	X	X	X	X
	L	X	X			X	X
	NIR	X	X	X	X	X	X
	T_s			X	X		
	ρ	X	X	X	X	X	
-50º	*SSA*	X	X	X	X	X	X
	E				X		
	HS	X	X	X	X	X	X
	L			X	X	X	

grain size) and the semiempirical extinction coefficient [see (28), using optical diameter calculated from SSA observations], as a series of eight (−40°) or nine (−50°) homogeneous layers. Layers had a range of physical temperatures (−0.4 °C to −6.2 °C), densities (80–322 kg · m^{-3}), SSA (7.4–42.9 m^2 · kg^{-1}), and grain size (0.25–3.0 mm). The underlying ground surface was characterized by its physical temperature (observed to be −0.83 °C by probe thermometers stationed across the IOA), as well as the permittivity of the ground, assumed to be $6 - 1j$ [11].

Fig. 10 shows a comparison of the SoRaX observed brightness temperatures with the simulations using the n-HUT model, utilizing the original extinction coefficient [Fig. 10(a)] and the newly derived extinction coefficient [Fig. 10(b)]. SoRaX n-HUT simulations were produced at 18.7, 21.0, and 36.5 GHz, at both H-Pol and V-Pol. Although the semiempirical extinction coefficient was calculated using only the V-Pol, the simulations were completed using both H-Pol and V-Pol for completeness. The results here on will focus purely on the V-Pol.

As the only difference between n-HUT models was the two extinction coefficient models, differences in simulated brightness temperatures were a direct result of the scattering coefficients; the theoretical absorption coefficient was equal for both n-HUT simulations. Differences in microstructure parameters [visual grain size for Fig. 10(a), and optical diameter derived from observations of SSA for Fig. 10(b)] affected the resulting scattering coefficient. Simulation RMSE (29) and bias (30) values were calculated for each frequency and polarization, and are displayed in Tables IV and V, respectively. Fig. 10(a) and (b) demonstrates improvements made to the

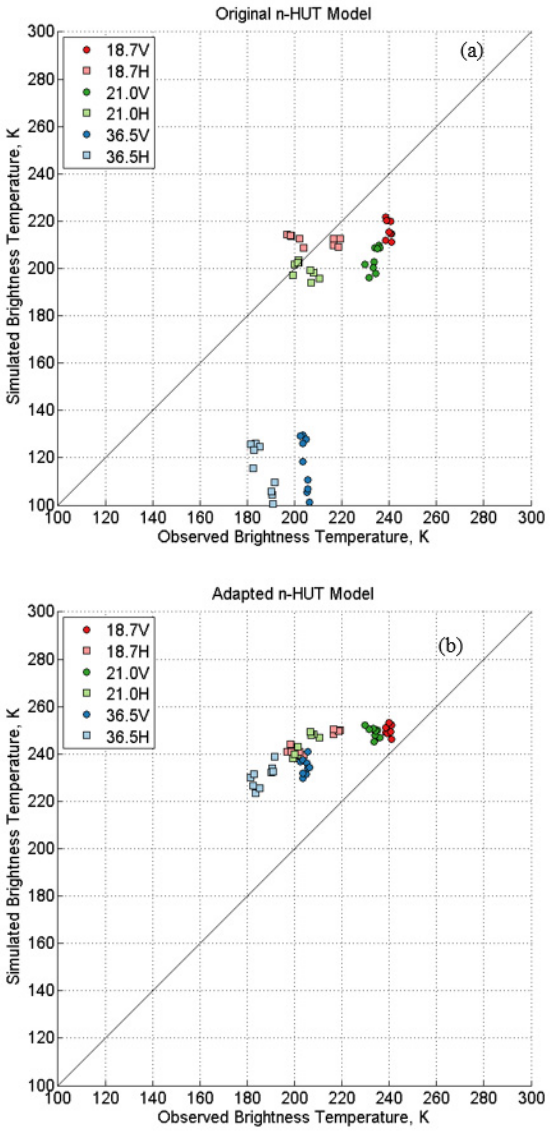


Fig. 10. n-HUT model simulations using the extinction coefficient using (a) traditional grain size and (b) D_o derived from SSA observations, at 18.7 (red), 21.0 (green), and 36.5 (blue) GHz, at H-Pol (square, pale) and V-Pol (circle, bold).

accuracy of the n-HUT model, especially at 36.5 GHz, when using the new extinction coefficient (28)

$$\text{RMSE} = \sqrt{\frac{\sum_1^n (T_{B,\text{sim}} - T_{B,\text{obs}})^2}{n}} \tag{29}$$

$$\text{Bias} = \frac{\sum_1^n (T_{B,\text{sim}} - T_{B,\text{obs}})}{n}. \tag{30}$$

Tables IV and V show the calculated RMSE and bias values at all frequencies and polarizations for both the extinction coefficients used. Magnitudes of RMSE and bias values decrease at V-Pols when using the new semiempirical extinction coefficient. An error reduction is also seen at H-Pol at 36.5 GHz; however, as the semiempirical extinction equation was derived using only V-Pols, no conclusions can be drawn.

Similar magnitudes of RMSE and bias values suggest that a large portion of the errors are due to a persistent bias present

TABLE IV

RMSE VALUES FOR THE SIMULATED BRIGHTNESS TEMPERATURES (K) OF THE SORAX SNOWPITS, FROM BOTH THE ORIGINAL AND ADAPTED N-HUT MODELS

Extinction Coefficient	Reference [10]		Equation (28)	
Freq. (GHz)	H-Pol	V-Pol	H-Pol	V-Pol
18.7	11.30	23.46	37.54	10.87
21.0	7.75	30.15	39.68	15.60
36.5	72.68	88.16	44.09	30.40

TABLE V

BIAS VALUES FOR THE SIMULATED BRIGHTNESS TEMPERATURES (K) OF THE SORAX SNOWPITS, FROM BOTH THE ORIGINAL AND ADAPTED N-HUT MODELS

Extinction Coefficient	Reference [10]		Equation (28)	
Freq. (GHz)	H-Pol	V-Pol	H-Pol	V-Pol
18.7	4.08	-23.08	37.12	10.62
21.0	-4.56	-29.88	39.63	15.17
36.5	-71.47	-87.36	43.98	30.22

TABLE VI

UNBIASED RMSE VALUES FOR THE SIMULATED BRIGHTNESS TEMPERATURES (K) OF THE SORAX SNOWPITS, FROM BOTH THE ORIGINAL AND ADAPTED N-HUT MODELS

Extinction Coefficient	Reference [10]		Equation (28)	
Freq. (GHz)	H-Pol	V-Pol	H-Pol	V-Pol
18.7	10.35	4.24	5.58	2.23
21.0	6.27	3.97	1.97	3.63
36.5	13.25	11.85	3.29	3.31

within the n-HUT model. This error is present regardless of the extinction coefficient used; a fact is shown in the unbiased RMSE values [see (31), Table VI]. Unbiased RMSE values have been calculated by subtracting bias values from observations and recalculating the RMSE values. Table VI shows a decrease in magnitude in unbiased RMSE values when using the new extinction coefficient. This improvement is highlighted at 36.5 GHz, where unbiased RMSE values decrease from 13.25 K (using the original extinction coefficient) at V-Pols to 3.29 K

$$\text{Unbiased RMSE} = \sqrt{\frac{\sum_1^n (T_{B,\text{sim}} - T_{B,\text{obs}} - \text{Bias})^2}{n}}. \quad (31)$$

A default value of $6 - 1j$ ([11]) was used for soil permittivity throughout. Values taken from [37] were used to assess the sensitivity of the unbiased RMSE values to the soil. The default value for soil permittivity was replaced with $3.42 - 0.005j$ and $4.47 - 0.33j$ at 18.7 and 36.5 GHz, respectively, and the simulations rerun. It was found that the unbiased RMSE values were insensitive to the change in soil permittivity, with a difference in unbiased RMSE values of $+0.5$ K at 18.7 GHz and -0.1 K at 36.5 GHz, across both the original and adapted n-HUT model simulations at H-Pol and V-Pol.

VI. DISCUSSION

The immediate implications of the utilization of the semiempirical extinction coefficient are twofold. First, the reduction of the simulation errors suggests that the accuracy of the n-HUT model is increased, allowing for improved simulations of microwave signatures of multiple-layer snowpacks; however, this reduction in simulated errors is slight and can only be discussed in the V-Pol.

Second, the inclusion of objectively-derived optical diameter as a viable input parameter into the n-HUT model facilitates the parameterization of microstructure size to take place via objective observations with increased precision relative to the conventional observer-based grain size estimation methods.

It should be noted that there are numerous errors surrounding the derivation and evaluation of the semiempirical extinction coefficient shown in this paper. Using the six-flux coefficient model with the ASMEx slab data produced a polarization difference between the six-flux horizontal and vertical scattering coefficients. This polarization difference was also presented in [33], where the model was originally produced. Similarly to [33], this study focused on the V-Pol when deriving the empirical scattering coefficient. This could be the reason behind the decrease in the accuracy of the H-Pol brightness temperature simulations by the n-HUT model.

During the ASMEx campaign, only three of the 14 measured slabs used all five available frequencies (as detailed by Maslanka *et al.* [31], [32]). This meant that the number of frequency observations was not consistent throughout ASMEx. The effects of the inconsistent number of frequency observations are apparent during the calculation of c_2 in Fig. 4(b). Measuring all slabs at all five frequencies would reduce the uncertainty caused by the differing number of observations at different frequencies and would allow for the influence of homogeneity [Fig. 4(a)] to be more pronounced.

The six-flux method of deriving the scattering coefficient is somewhat inconsistent with the strongly forward scattering assumption within n-HUT. Despite this, the intermediate evaluation of the new extinction coefficient model showed improved RMSE and bias in comparison with the original method determined via transmission experiments that are more physically compatible with the radiative transfer solution method in n-HUT. The improvement given by the objective microstructure as an input into the n-HUT model (rather than the subjective traditional grain size measurement) more than compensates for the difference in treatment of fluxes

and further improvements may be obtained by revisiting the strongly forward scattering assumption within n-HUT. The improvements are small for the slabs, but this is to be expected given the thinness of the slabs and therefore small amount of scattering material. The larger improvement in RMSE and bias at 89.0 GHz can be accredited to the extended frequency range that the semiempirical extinction coefficient model offers (18.7–89.0 GHz) over the original (18–60 GHz).

The SoRaX data set was primarily used to demonstrate the improvement in the adapted n-HUT model. The surface roughness of the SoRaX data set was estimated through the use of the NIR photography (primarily used to determine snowpack stratigraphy). Any errors and uncertainties within the soil roughness estimations could have resulted in the errors in simulated brightness temperature. In addition to this, the soil permittivity was assumed to be constant across all snow pits. Assuming that all snow pits exhibited the same soil permittivity may have introduced errors into the soil reflectivity [38], resulting in uncertainties in the simulated brightness temperatures. However, simulation tests showed that changing the permittivity value within realistic values for frozen soil had only a minimal effect on results.

Fig. 10(a) displays a general underestimation of brightness temperatures at 36.5 GHz, corroborating results by Pan *et al.* [14], suggesting underestimation of brightness temperature using the original n-HUT model for deep snow (snow depth was already 1 m on average during the pit excavation of SoRaX). Use of the new formulation of extinction coefficient reduces these underestimations [Fig. 10(b)], leading to a slight overestimation of brightness temperature across all frequencies and polarizations. This suggests that the new formulation may mitigate the limitations of the one-flux formulation in the n-HUT model, which was perceived as the main source of underestimation by Pan *et al.* [14]. However, further studies including measurements of deeper snow would be needed to ascertain this. Moreover, Pan *et al.* [14] applied the measurement of E as inputs into the n-HUT and Microwave Emission Model of Layered Snowpacks (MEMLS) models, making it difficult to directly compare with results here.

A possible area of future work would be to improve upon the semiempirical extinction coefficient presented here, through the use of an optical diameter scaling parameter, to better optimize the extinction coefficient and to better model the level of scattering taking place. An additional area of future work would be to compare the adapted n-HUT model with other microwave snow emission models, such as the MEMLS [39], the Dense Media Radiative Theory (DMRT, [40]) model, and the Snow Microwave Radiative Transfer (SMRT, [41]) model, using the SoRaX data set, to assess the differences across the models.

The improved parameterization of model extinction coefficient improves the overall model formulation and increases the accuracy of the brightness temperature simulations for the data sets used. It is anticipated that when coupled with energy and mass balance models that incorporate detailed microstructure parameters (such as D_o), improved simulations will be realized. The improvements also have implications for approaches that combine ground, airborne, or satellite-based observations, through data assimilation schemes, to better estimate global snow mass and SWE.

VII. Conclusion

Semiempirical microwave emission models have been used in conjunction with passive microwave remote sensing data, in order to extract global snow mass and SWE from satellite data. This paper presents the derivation of a semiempirical extinction coefficient model, for use with the n-HUT model, utilizing objective calculations of optical diameter instead of the traditionally used grain size E. The semiempirical extinction coefficient model was derived using a six-flux coefficient model, using data collected as part of the ASMEx campaign. Both the original and the semiempirical extinction coefficient were used with the n-HUT model to simulate the brightness temperature of a naturally evolved, multilayer snowpack observed during the separate SoRaX campaign on the following year, at 18.7, 21.0, and 36.5 GHz. The results from this study show that using the semiempirical coefficient model in conjunction with data collected from SoRaX produced more accurate simulations of the microwave signature of a multiple-layered snowpack at V-Pols than with the previous empirical formulation of the extinction coefficient, and produced lower unbiased RMSE values at both polarizations. Future work into the source of the polarization difference in retrieved scattering coefficient will ultimately lead to further improvement to the accuracy of the semiempirical extinction coefficient and, thus, the simulated brightness temperatures from the n-HUT model at both polarizations. The data and methodologies applied here could potentially benefit the development and evaluation of other similar models as well.

Acknowledgment

The authors would like to thank the staff of the Arctic Research Centre, Finnish Meteorological Institute (FMI), Sodankylä, Finland, for performing the ground-based radiometer measurements and macro- and microstructure measurements for both the ASMEx and the SoRaX campaigns. They would like to thank the staff of the WSL Institute for Snow and Avalanche Research SLF, Davos, Switzerland, for the SMP instrument and for the SMP and μCT analyses of the snow samples. They would also like to thank two anonymous reviewers whose comments have helped improve this paper greatly.

References

[1] J. Cohen and D. Rind, "The effect of snow cover on the climate," *J. Climate*, vol. 4, pp. 689–706, Jul. 1991.

[2] T. P. Barnett, J. C. Adam, and D. P. Lettenmaier, "Potential impacts of a warming climate on water availability in snow-dominated regions," *Nature*, vol. 438, no. 7066, pp. 303–309, Nov. 2005.

[3] A. T. C. Chang, J. Foster, and D. K. Hall, "Nimbus-7 SMMR derived global snow cover parameters," *Ann. Glaciol.*, vol. 9, pp. 39–44, 1987.

[4] J. P. Hollinger, J. L. Peirce, and G. A. Poe, "SSM/I instrument evaluation," *IEEE Trans. Geosci. Remote Sens.*, vol. 28, no. 5, pp. 781–790, Sep. 1990.

[5] R. E. Kelly, A. T. Chang, L. Tsang, and J. L. Foster, "A prototype AMSR-E global snow area and snow depth algorithm," *IEEE Trans. Geosci. Remote Sens.*, vol. 41, no. 2, pp. 230–242, Feb. 2003.

[6] M. Takala, J. Pulliainen, S. J. Metsamaki, and J. T. Koskinen, "Detection of snowmelt using spaceborne microwave radiometer data in eurasia from 1979 to 2007," *IEEE Trans. Geosci. Remote Sens.*, vol. 47, no. 9, pp. 2996–3007, Sep. 2009.

[7] J. L. Foster, D. K. Hall, and A. T. C. Chang, "Remote sensing of snow," *EOS, Trans. Amer. Geophys. Union*, vol. 68, no. 32, pp. 682–684, 1987.

[8] J. Foster *et al.*, "Quantifying the uncertainty in passive microwave snow water equivalent observations," *Remote Sens. Environ.*, vol. 94, no. 2, pp. 187–203, Jan. 2005.

[9] A. T. C. Chang, R. E. J. Kelly, E. G. Josberger, R. L. Armstrong, and N. M. Mognard, "Analysis of ground-measured and passive-microwave-derived snow depth variations in midwinter across the northern great plains," *J. Hydrometeorol.*, vol. 6, no. 1, pp. 20–33, 2005.

[10] M. Hallikainen, F. T. Ulaby, and T. Van Deventer, "Extinction behavior of dry snow in the 18-to 90-GHz range," *IEEE Trans. Geosci. Remote Sens.*, vol. GE-25, no. 6, pp. 737–745, Nov. 1987.

[11] J. T. Pulliainen, J. Grandell, and M. T. Hallikainen, "HUT snow emission model and its applicability to snow water equivalent retrieval," *IEEE Trans. Geosci. Remote Sens.*, vol. 37, no. 3, pp. 1378–1390, May 1999.

[12] J. Lemmetyinen, J. Pulliainen, A. Rees, A. Kontu, Y. Qiu, and C. Derksen, "Multiple-layer adaptation of HUT snow emission model: Comparison with experimental data," *IEEE Trans. Geosci. Remote Sens.*, vol. 48, no. 7, pp. 2781–2794, Jul. 2010.

[13] F. Vachon, K. Goita, D. De Seve, and A. Royer, "Inversion of a snow emission model calibrated with *in situ* data for snow water equivalent monitoring," *IEEE Trans. Geosci. Remote Sens.*, vol. 48, no. 1, pp. 59–71, Jan. 2010.

[14] J. Pan *et al.*, "Differences between the HUT snow emission model and MEMLS and their effects on brightness temperature simulation," *IEEE Trans. Geosci. Remote Sens.*, vol. 54, no. 4, pp. 2001–2019, Apr. 2016.

[15] C. Mätzler, "Applications of the interaction of microwaves with the natural snow cover," *Remote Sens. Rev.*, vol. 2, no. 2, pp. 259–387, 1987.

[16] C. Matzler, "Microwave properties of ice and snow," in *Solar System Ices*, vol. 227, B. Schmitt, C. De Bergh, and M. Festou, Eds., 1st ed. Dordrecht, The Netherlands: Springer, 1998, pp. 241–257.

[17] C. R. Fierz *et al.*, "The international classification for seasonal snow on the ground," IHP-VII, Paris, France, Tech. Rep. 1, 2009, pp. 1–80.

[18] L. Leppänen, A. Kontu, H.-R. Hannula, H. Sjöblom, and J. Pulliainen, "Sodankylä manual snow survey program," *Geosci. Instrum., Methods Data Syst.*, vol. 5, no. 1, pp. 163–179, May 2016.

[19] B. Montpetit *et al.*, "*In-situ* measurements for snow grain size and shape characterization using optical methods," in *Proc. 68th Eastern Snow Conf.*, 2011, pp. 173–188.

[20] L. Leppänen, A. Kontu, J. Vehviläinen, J. Lemmetyinen, and J. Pulliainen, "Comparison of traditional and optical grain-size field measurements with SNOWPACK simulations in a taiga snowpack," *J. Glaciol.*, vol. 61, no. 225, pp. 151–162, 2015.

[21] C. M. Carmagnola *et al.*, "Implementation and evaluation of prognostic representations of the optical diameter of snow in the SURFEX/ISBA-Crocus detailed snowpack model," *Cryosphere*, vol. 8, no. 2, pp. 417–437, 2014.

[22] L. Legagneux, A. Cabanes, and F. Dominé, "Measurement of the specific surface area of 176 snow samples using methane adsorption at 77 K," *J. Geophys. Res.*, vol. 107, no. D17, pp. ACH 5-1–ACH 5-15, 2002.

[23] B. Montpetit *et al.*, "New shortwave infrared albedo measurements for snow specific surface area retrieval," *J. Glaciol.*, vol. 58, no. 211, pp. 941–952, 2012.

[24] J.-C. Gallet, F. Domine, C. S. Zender, and G. Picard, "Measurement of the specific surface area of snow using infrared reflectance in an integrating sphere at 1310 and 1550 nm," *Cryosphices*, vol. 3, no. 2009, pp. 167–182, 2009.

[25] N. Zuanon, "IceCube, a portable and reliable instruments for snow specific surface area measurement in the field," in *Proc. Int. Snow Sci. Workshop Grenoble-Chamonix Mont-Blance*, 2013, pp. 1020–1023.

[26] M. Schneebeli, C. Pielmeier, and J. B. Johnson, "Measuring snow microstructure and hardness using a high resolution penetrometer," *Cold Regions Sci. Technol.*, vol. 30, nos. 1–3, pp. 101–114, 1999.

[27] M. Proksch, N. Rutter, C. Fierz, and M. Schneebeli, "Intercomparison of snow density measurements: Bias, precision, and vertical resolution," *Cryosphere*, vol. 10, pp. 371–384, Feb. 2016.

[28] M. Proksch, H. Löwe, and M. Schneebeli, "Density, specific surface area, and correlation length of snow measured by high-resolution penetrometry," *J. Geophys. Res.-Earth Surf.*, vol. 120, no. 2, pp. 346–362, 2015.

[29] M. Schneebeli and S. A. Sokratov, "Tomography of temperature gradient metamorphism of snow and associated changes in heat conductivity," *Hydrol. Process.*, vol. 18, no. 18, pp. 3655–3665, 2004.

[30] M. Heggli, E. Frei, and M. Schneebeli, "Snow replica method for three-dimensional X-ray microtomographic imaging," *J. Glaciol.*, vol. 55, no. 192, pp. 631–639, 2009.

[31] W. Maslanka *et al.*, "Arctic snow microstructure experiment for the development of snow emission modelling," *Geosci. Instrum., Methods Data Syst.*, vol. 5, no. 1, pp. 85–94, 2016.

[32] W. M. Maslanka, "Extinction of microwave radiation in snow," Dept. Meteorol., Univ. Reading, Reading, U.K., 2017, p 237.

[33] A. Wiesmann, C. Mätzler, and T. Weise, "Radiometric and structural measurements of snow samples," *Radio Sci.*, vol. 33, no. 2, pp. 273–289, 1998.

[34] A. M. Toure, K. Goïta, A. Royer, C. Mätzler, and M. Schneebeli, "Near-infrared digital photography to estimate snow correlation length for microwave emission modeling," *Appl. Opt.*, vol. 47, no. 36, pp. 6723–6733, 2008.

[35] M. Hallikainen, F. Ulaby, and M. Abdelrazik, "Dielectric properties of snow in the 3 to 37 GHz range," *IEEE Trans. Antennas Propag.*, vol. AP-34, no. 11, pp. 1329–1340, Nov. 1986.

[36] K. D. Tape, N. Rutter, H. P. Marshall, R. Essery, and M. Sturm, "Recording microscale variations in snowpack layering using near-infrared photography," *J. Glaciol.*, vol. 56, no. 195, pp. 75–80, Apr. 2010.

[37] B. Montpetit, A. Royer, A. Roy, and A. Langlois, "*In-situ* passive microwave emission model parameterization of sub-arctic frozen organic soils," *Remote Sens. Environ.*, vol. 205, pp. 112–118, Feb. 2018.

[38] A. Roy *et al.*, "Brightness temperature simulations of the Canadian seasonal snowpack driven by measurements of the snow specific surface area," *IEEE Trans. Geosci. Remote Sens.*, vol. 51, no. 9, pp. 4692–4704, Sep. 2013.

[39] A. Wiesmann and C. Mätzler, "Microwave emission model of layered snowpacks," *Remote Sens. Environ.*, vol. 70, no. 3, pp. 307–316, 1999.

[40] G. Picard *et al.*, "Simulation of the microwave emission of multi-layered snowpacks using the dense media radiative transfer theory: The DMRT-ML model," *Geosci. Model Develop.*, vol. 6, no. 4, pp. 1061–1078, 2013.

[41] G. Picard, M. Sandells, and H. Löwe, "SMRT: An active–passive microwave radiative transfer model for snow with multiple microstructure and scattering formulations (v1.0)," *Geosci. Model Device*, vol. 11, pp. 2763–2788, Jul. 2018.



William Maslanka received the MMet degree in meteorology, with a year in Oklahoma, and the Ph.D. degree in remote sensing of snow from the University of Reading, Reading, U.K., in 2013 and 2017, respectively.

His research interests include microwave remote sensing, *in situ* and remote sensing observations of snow, and hydrological processes.



Melody Sandells received the M.Sc. degree in physics from Imperial College London, London, U.K., in 1998, and the Ph.D. degree from the University of Reading, Reading, U.K. in 2002.

She is currently the Director of the Center for Open Research (CORES) Science and Engineering Limited, Burnopfield, U.K. Her research interests include snow and cryosphere physics, earth observation of snow and soil moisture, and soil–snow–vegetation radiative transfer at optical, thermal, and microwave wavelengths.



Robert Gurney was the Head of the Hydrological Sciences Branch, NASA Goddard Space Flight Centre, Greenbelt, MD, USA, where he was also the Director of the Environmental Systems Science Centre, for 18 years. He is currently a Professor of earth observation science with the University of Reading, Reading, U.K. He has recently jointly chaired the Data and Information Systems Collaborative Research Action of the Belmont Forum to further this aim. His research interests include the use of remote sensing to understand hydrological processes at the land surface and bringing together multiple data sets to understand the earth system.



Juha Lemmetyinen received the D.Sc. (Tech) degree in electrical engineering from Aalto University (formerly known as Helsinki University of Technology, TKK), Espoo, Finland, in 2012.

From 2004 to 2008, he was a Researcher with the TKK Laboratory of Space Technology, Department of Radio Science and Engineering, Helsinki University of Technology, where he specialized in radiometer calibration techniques and remote sensing. From 2009 to 2013, he was a Scientist with the Arctic Research Unit, Finnish Meteorological Institute, Helsinki, Finland, where he has been the Head of Group for research on cryosphere processes, since 2014. His research interests include applications of microwave radiometers and synthetic aperture radar in remote sensing snow, and soil and vegetation, including the development of emission and backscatter models.



Leena Leppänen received the M.Sc. degree in astronomy from the University of Oulu, Oulu, Finland, in 2012. She is currently pursuing the Ph.D. degree with the University of Helsinki, Helsinki, Finland.

Since 2012, she has been a Research Scientist with the Space and Earth Observation Centre, Finnish Meteorological Institute, Sodankylä, Finland. Her research interests include *in situ* and remote sensing observations of snow.



Anna Kontu received the M.Sc. (Tech.) degree from the Helsinki University of Technology (currently part of Aalto University), Espoo, Finland, in 2006, and the D.Sc. (Tech.) degree from Aalto University, Espoo, in 2018.

She is currently a Sodankylä Research Infrastructure PI with the Arctic Space Centre, Finnish Meteorological Institute, Sodankylä, Finland. Her research interests include the microwave remote sensing of seasonal terrestrial snow and soil frost.

Margret Matzl, photograph and biography not available at the time of publication.



Nick Rutter received the D.Phil. degree in subglacial water storage in an alpine glacier from the School of Geography, University of Oxford, Oxford, U.K., in 2002.

From 2002 to 2005, he was a Post-Doctoral Research Fellow, evaluating methods of snowpack observation (*in situ* and remote sensing) and modeling while employed on the NASA Cold Land Processes Experiment by the University Corporation for Atmospheric Research based at the National Hydrologic Remote Sensing Center, Chanhassen, MN, USA. From 2005 to 2007, he was an NERC Post-Doctoral Research Assistant with Aberystwyth University, Aberystwyth, U.K., where he evaluated approaches to snowpack modeling under forest canopies (SnowMIP2). From 2007 to 2009, he was an NERC Post-Doctoral Research Fellow with The University of Sheffield, Sheffield, U.K., where he was involved in improving current and future satellite observations of snow water equivalent. In 2009, he was appointed as a Senior Lecturer with the Department of Geography and Environmental Sciences, Northumbria University, Newcastle upon Tyne, U.K., where he is currently an Associate Professor.

Tom Watts, photograph and biography not available at the time of publication.



Richard Kelly received the Ph.D. degree in geography from the University of Bristol, Bristol, U.K., in 1995.

He held academic and research positions at the University of London, London, U.K., and the NASA Goddard Space Flight Centre (GSFC), Greenbelt, MD, USA. He is the PI for JAXA's AMSR2 standard snow depth product and has extensive experience in satellite microwave analysis of the cryosphere and field experiments using ground-based microwave systems in cold season environments. He is currently a Professor of physical geography with the University of Waterloo, Waterloo, ON, Canada. His research interests include the microwave remote sensing of snow and ice.

Dr. Kelly is a member of AGU and the IEEE Geoscience and Remote Sensing Society. He was the President of the Eastern Snow Conference.